Construction and Building Materials 457 (2024) 139330

Contents lists available at ScienceDirect

Construction and Building Materials

journal homepage: www.elsevier.com/locate/conbuildmat

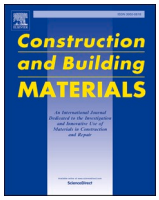

Mechanisms of air bubble rise in cement suspensions studied by X-ray analysis

Bastian Strybny [a,*], Julian Link [a], Max Coenen [a], Valérie Vidal [b], Marcus Zuber [c], Tobias Schack [a], Michael Haist [a]

[a] Institute of Building Materials Science, Leibniz University Hannover, Germany
[b] Laboratoire de Physique, ENS de Lyon, CNRS, France
[c] Institute for Photon Science and Synchrotron Radiation, Karlsruhe Institute of Technology, Germany

ARTICLE INFO

Keywords:
De-airing
Air bubble rise
Cement suspensions
Particle migration
Rheology
X-ray

ABSTRACT

The de-airing of fresh concrete is a crucial step in ensuring sustainable and durable concrete structures. Currently, proper de-airing is ensured by adjusting the fresh concrete consistency i.e. its rheological properties, without any knowledge whether this will actually guarantee sufficient de-airing. The exact relationship between the rheological properties and air bubble dynamics in concrete is not yet understood. In this paper, a detailed study was carried out in which air bubbles of different size and volume were injected in fresh cement suspensions with varying solid volume fractions (i.e. varying rheological behaviour). The air bubbles were visualised by means of X-ray radiography and the rise behaviour was evaluated with image based algorithms. It was found that in more viscous suspensions (i.e. higher particle contents) the bubble speed increases with decreasing suspension viscosity. For suspensions with higher flowability (i.e. less particle content), the inertial forces dominate the viscous forces, with the viscosity playing a subordinate role. The shear rate induced by an ascending air bubble is sufficient to locally reduce the dynamic viscosity of the suspension. In addition, it leads to shear-induced particle migration, with less concentrated regions in the ascending channel. Consequently, subsequent bubbles are influenced by changes of viscosity in this channel, rising faster and having different bubble shapes.

1. Introduction

Insufficient de-airing during compaction and subsequent formation of air void clusters and cavities in the hardened building member can be considered as one of the most decisive problems in concrete casting, leading to a reduction in strength and durability and increasing the risk of crack formation. Air voids arise both from the mixing of the dry constituents, from the concrete transport and conveying and especially from the placing of the fresh concrete. Both the typical size of air bubbles (before compaction) as well as the air void content however are unknown. Fundamental work has been performed on the concrete compaction behaviour in the past [1–5]. However, the current literature focusses mainly on the correlation between the changes in rheology during concrete compaction by vibration [3,6] or how vibrations are propagated within the radius of action during internal poker compaction [7,8]. Other authors consider the destructive consequences of over-excessive vibration and how segregation occurs for different aggregate granulometries [9,10]. Overall, there is in agreement in the literature that a proper compaction depends on the fresh concrete properties, which are controlled by its rheology. Further, it is well documented that concrete rheology is directly related to the cement paste rheology [11] as well as the paste content and grading curve of the aggregates [12]. With regard to the paste rheology, this is primarily controlled by the content and the properties (e.g. chemical reactivity, intrinsic packing density, solid volume fraction etc.) of the cement particles as well as the content and mode of action of admixtures contained therein. Typically, cement pastes exhibit a pronounced non-Newtonian flow behaviour [13] which can most simplistically be described by the Bingham- or the Herschel-Bulkley models [14], superimposed by very pronounced thixotropic effects and a substantial shear history dependence [15,16].

Despite the importance of cement paste and concrete rheology for de-airing, their influence on air bubble movement in such cementitious systems has to the understanding of the authors hardly been investigated. Analogies to other research fields however can be drawn when cement paste is idealized as a homogeneous, non-granular substance

* Correspondence to: Institut für Baustoffe, Appelstraße 9A, Hannover 30167, Germany.
E-mail address: b.strybny@baustoff.uni-hannover.de (B. Strybny).

https://doi.org/10.1016/j.conbuildmat.2024.139330
Received 26 September 2024; Received in revised form 28 October 2024; Accepted 22 November 2024
Available online 3 December 2024

Table 1
Oxidic composition of the cement measured by the XRF method.

Component	CaO	SiO_2	Al_2O_3	Fe_2O_3	MgO	K_2O	Na_2O	TiO_2	P_2O	Mn_2O_3	SO_3	LOI	Cl^-	Sum
	[wt%]													
CEM I 42.5 R	61.79	21.14	5.53	2.27	1.39	0.77	0.77	0.21	0.14	0.03	2.84	2.48	0.03	98.94

with non-Newtonian properties. Pioneering work was e.g. presented by Clift et al. [17] and further extended by Harper [18] and Maxworthy et al. [19]. The rise of a single bubble in a homogeneous fluid is here mainly described by two flow regimes, the viscous flow regime and the inertial flow regime. In the viscous regime, the bubble speed is essentially determined by the dynamic viscosity of the fluid, whereas in the inertial regime, inertial forces dominate. The transition between these two regimes can be described as a function of the Reynolds number Re (see Eq. 1), which defines the balance between inertial and viscous forces. Here ρ designates the density of the fluid, v is the steady state bubble rise speed, r_{eff} is the effective radius of a spherical bubble with the same size and η is the dynamic viscosity of the liquid.

$$\mathrm{Re} = \frac{\rho \bullet v \bullet r_{eff}}{\eta} \quad (1)$$

[17–19] also conclude that the flow state (i.e. inertial vs. viscous regime) also reflects in the shape and here especially in the aspect ratio χ (i.e. bubble height vs. bubble width) of the bubble. Bubbles tend to exhibit a predominantly flat shape ($\chi < 1$) in the inertial regime and transition to a more elliptical, droplet-shaped appearance ($\chi \geq 1$) in the viscous regime.

Astarita and Apuzzo [20], investigated the influence of different polymer concentrations in Carbopol (i.e. different rheological properties, including the existence of a yield-stress) on bubble motion and found that the bubble size, shape and velocity are strongly affected by the rheological properties of the fluid. Building on this, Dubash and Frigaard [21,22] studied the minimal bubble size required to start a rising movement and the boundary conditions needed for static bubble stagnation, in principal confirming the inertial and the visous regimes. The changes in bubble shape by varying fluid properties were also investigated numerically by Tripathi et al. [23] and Tsamopoulos et al. [24]. These authors pointed out that the fluid in the direct vicinity of the bubble is subjected to a shear zone. Lopez et al. [25] addressed the influence of the shear history on the bubble trajectory by creating a sheared zone at a tiled angle to the vertical axis and in doing so showing that this artificial shearing zone creates a favourable path for rising bubbles in such a way, that the bubbles even rise at an angle. Mougin et al. [26] were able to show the same phenomenon, but they injected a second bubble after the first one and observed that the subsequent bubble followed the same path, but with an altered shape (i.e. the bubble becomes longer in the direction of the path). It has also been pointed out that bubble motion in shear thinning fluids, such as cementitious systems, leads to very complex shear rate and viscosity distributions in the close vicinity of the bubble, but these effects have not been linked to particle migration and irreversible fluidization [27–29].

Although cement paste can be described with such model fluids, it is important to note that the properties of polydisperse cement particle suspensions deviate significantly from those of homogeneous fluids such as Carbopol, very likely also affecting the air bubble rise behaviour. Here, the number of studies in the literature on bubble movement in granular suspensions is extremely small. Hooshyar et al. [30] investigated the rise of single bubbles in liquid-solid suspensions using an X-ray transmission analysis. The study included varying particle sizes in monodisperse distributions, but the maximum solid volume fraction was limited to 0.20, thus not being comparable to a densely packed cement suspensions. The results however give a clear hint that the bubble rise behaviour changes, depending on the size and concentration of solid particles compared to the pure liquid. Another way to visualise bubble flow in granular suspensions is by using a Hele-Shaw cell, namely two glass plates separated by a thin gap. Madec et al. [31] investigated suspensions of spherical, neutrally buoyant and non-Brownian particles and clearly proved the existence of a shear thinning of the carrier liquid in the bubble region and local, irreversible particle migration in the uprising path of the bubble. The results were modelled with the so-called Suspension Balance Model (SBM), yet the flow processes in a Hele-Shaw cell cannot be fully transferred to the 3D scenario.

With regard to concrete, Auernhammer et al. [32] developed a transparent model concrete consisting of glass spheres suspended in a yield stress fluid made from Carbopol which allowed for tuning the rheological properties to be comparable to those of real cementitious suspensions or concretes. The focus of their study was on particle migration during pumping of the model concrete, rather than on air bubble formation and bubble movement.

To summarise the current state of research, whereas the compaction behaviour of fresh concrete has been studied in the literature, here focussing primarily on the liquefaction and rheological changes of the concrete during vibration, only very little information is available on the mechanisms of air bubble rise in rheologically and granulometrically complex media such as concrete. There is substantial reason for doubt, whether the bubble rise observed in homogenous (transparent) model fluids such as Carbopol, underlies the same mechanisms as in concrete. This paper explicitly addresses how different air bubble volumes rise in 3D in opaque granular cement suspensions using combined X-ray techniques for imaging. It focuses on the influence of the rheological properties and the shear thinning behaviour of cement suspensions with different cement solid volume fractions on the de-airing behaviour. The objective of this paper was to investigate the fundamentals of air bubble rise in cement suspensions. The results give a first basis for further investigations in this field, e.g. numerical simulations or modeling of concrete de-airing.

Table 2
Composition of investigated cement suspensions.

Solid volume fraction ϕ	Mass cement $m_{cem.}$	Mass water $m_{cem.}$	water-to-cement ratio w/c
[-]	[g]	[g]	[-]
0.36	3391	1920	0.57
0.38	3580	1860	0.52
0.40	3768	1800	0.48
0.42	3956	1740	0.44

2. Materials and methods

2.1. Raw materials

In this study, Ordinary Portland Cement CEM I 42.5 R (HeidelbergCement AG, Plant Ennigerloh, Germany) was used to prepare the cement suspension. The material was provided by the German DFG Priority Program DFG SPP 2005 program 'Opus Fluidum Futurum – Rheology of reactive, multiscale, multiphase construction materials'. The density (EN 1097–7: 2008 [33]) of the cement was 3.14 g/cm^3 and the specific surface area (SSA) measured by the BET method (ISO 9277: 2014 [34]) was 1.04 m^2/g and the SSA measured by Blaine method (EN196–6: 2019 [35]) was 3500 cm^2/g. The polydisperse particle size distribution is given with d_{10}=1.92 µm, d_{50}=14.10 µm and d_{90}=41.49 µm. The oxidic composition is shown in Table 1. Further

Table 3
Mixing procedure.

Time	Step description	Duration
[min]		[sec]
0–0:30	Pouring and mixing of components by hand	30
0:30–1:30	Mixing at lower speed	90
1:30–3:00	Manual return of caking material	90
3:00–4:30	Mixing at higher speed	90
4:30–5:00	Manual return of caking material	30
5:00–6:00	Mixing at higher speed	60
6:00–12:30	Rest	390
12:30–13:00	Re-mixing at lower speed	30

details can be found in [36].

2.2. Suspension preparation

The suspensions were prepared by mixing the cement with water with different solid volume fractions ϕ and corresponding water-to-cement ratios (see Table 2). The solid volume fraction was varied in four steps from ϕ=0.36 to ϕ=0.42. This variation results in water-to-cement ratios ranging from w/c = 0.57 to w/c = 0.44, which are typical for concrete applications. For each batch 3 dm^3 of fresh cement paste were prepared. The suspension temperature was adjusted to 20 ± 2 °C by pre-tempering the deionized water to 10°C before mixing. The cement was stored at 20 ± 2 °C.

After adding the cement to the water and mixing it with a trowel by hand for 30 s, a mechanical whisk mixer was used. The rotational speed of the whisk was adjusted in a stepwise manner: After 90 s at low speed, the mixture was manually mixed by hand again to dissolve any material stuck to the bottom of the vessel before mixing it again with the whisk at higher speed. These two steps were repeated and the sample was kept covered for a resting time of 390 s at 20 ± 2 °C. After a short re-mixing for 30 s at lower speed, the 13 min sample preparation was complete and the de-airing measurements were started after 15 min of water-cement contact. The detailed mixing procedure is shown in Table 3 and follows to the cement paste mixing procedure developed in [37].

2.3. Suspension characterization

Immediately after mixing the spread flow test acc. to [38] was performed. For suspensions with higher flowability (i.e. spread flow diameter > 200 mm), Eq. 2 can be used to compute the yield stress $\tau_{0,slump}$ from the measured flow radius R, the cone volume Ω, the gravity g and the sample density ρ [39,40].

$$\tau_{0,slump} = \frac{225 \bullet \rho \bullet g \bullet \Omega^2}{128 \bullet \Pi^2 \bullet R^5} \quad (2)$$

Rheological measurements were carried out using a HAAKE MARS 60 rheometer (ThermoFisher Scientific, Karlsruhe, Germany). The measurement geometry was a vane-in-cup geometry with a window-shaped paddle geometry (see geometry No. P-3 in [37]) in a cylindrical building materials cell and the measuring gap between the rotor and the bottom was set to 10 mm. The measurement sequence consisted of a rotational speed-controlled ramp consisting of a continuous increase of shear rate until a value of 80 s^{-1} followed by a plateau. The profile terminates with a stepwise decrease in shear rate to determine the flow curve. Each step of constant shear rate lasted 20 seconds, but only the mean value of the shear stress within the last second of each step was used to determine the dynamic viscosity in a steady state. The Bingham parameters yield stress $\tau_{0,rheo}$ and plastic viscosity μ_{rheo} were calculated by linear regression of the flow curve in the shear rate range between 20 s^{-1} and 80 s^{-1}. Further details regarding the measurement device, geometry and the calculations can be found in [37,41].

In addition to the rheological characterization, the surface tension, which is one of the key parameters for describing the process of rising air bubbles in fluids, was determined. It describes the interfacial tension between a fluid and a gas. In this study, surface tension measurements are performed optically using the pendant drop method with an ATTENSION THETA FLOW tensiometer (Biolin Scientific, Goeteborg, Sweden). A defined volume of cement suspension herefore was delivered via a pipette, forming a drop so that the suspension is in direct interaction with the surrounding air. It is important that the drop has a droplet or pendant shape and that the shape is not affected by the pipette itself. Eq. 3 can be used to calculate the surface tension of the drop from the difference in density between suspension and air $\Delta\rho$, the gravity g, the radius of curvature at the apex R_0 and a shape factor β defined by the Young-Laplace equation.

$$\gamma = \frac{\Delta\rho \bullet g \bullet R_0}{\beta} \quad (3)$$

2.4. X-ray transmission based de-airing measurement

In this study, we investigate the movement of a single air bubble in a fresh cement suspension by means of optical investigations. For this purpose, a new test setup was developed that allows a quantification of bubble properties such as bubble speed, bubble shape, trajectory etc., by using X-ray radiography. X-ray imaging was carried out at the Institute for Photon Science and Synchrotron Radiation (IPS), Karlsruhe Institute of Technology, Germany. The novel de-airing test setup consists of a

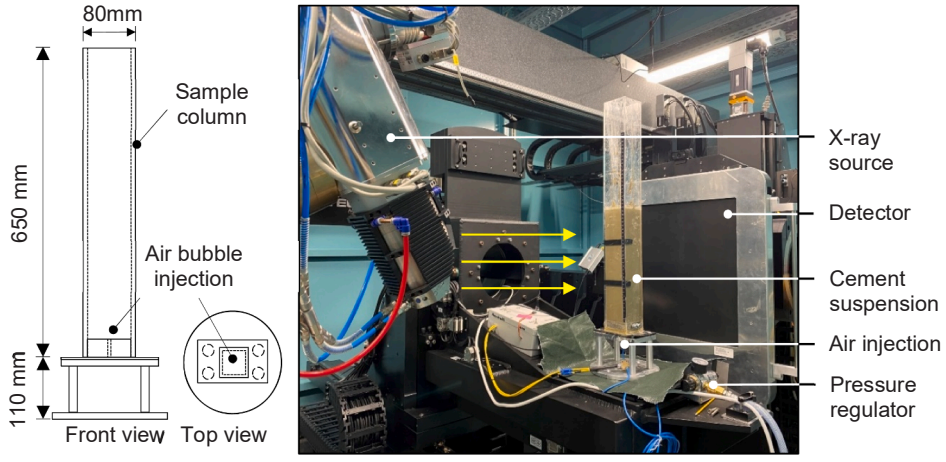

Fig. 1. Schematic drawing of the sample column (left) and experimental setup in the X-ray laboratory at IPS KIT (right).

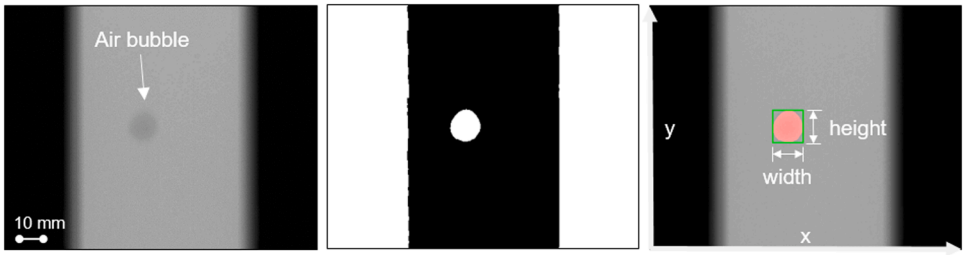

Fig. 2. Recorded raw image (left), after image segmentation (middle) and overlayed with bounding box (right) of an air bubble in cement suspension (ϕ=0.38).

Table 4
Material characterization of cement suspensions.

Solid volume fraction ϕ	Yield stress $\tau_{0,rheo}$	Plastic viscosity μ_{rheo}	Spread flow SF	Slump yield stress [Eq. 2] $\tau_{0,slump}$	Surface tension γ_{mean}	Cal. Density ρ
[-]	[Pa]	[Pa s]	[mm]	[Pa]	[mN/m]	[kg/dm^3]
0.36	6.18	0.14	325.0	3.23	34.6	1.77
0.38	10.64	0.18	260.0	10.10	33.9	1.81
0.40	27.28	0.27	227.5	20.15	38.3	1.86
0.42	46.26	0.47	197.5	44.56	31.7	1.90

rectangular Plexiglas column measuring 650 mm in height with a clear inner cross-section of 75 ×75 mm^2 and a wall thickness of 5 mm, see Fig. 1. The column is mounted to a base plate and placed between the X-ray source and the detector. The sample column can be moved in vertical and horizontal directions to ensure the required alignment for image acquisition. Air bubbles are injected into the cement suspension through a 5 mm diameter tube on the bottom. The air injection is carried out using compressed air, the air pressure is set to 1 bar via a pressure regulator and the injection process is flow rate controlled via a high-precision magnet valve. The valve opening duration is electrically controlled using an Arduino board, which is connected to the X-ray device. The delay period of the valve is 10 ms. The air injection command triggers the X-ray beam image capture and the image acquisition is automatically started. The X-ray source operated at a target power of 280 W and 220 kV at a 30 Hz frame rate. The resolution of the CT scans was 0.28 mm per pixel. Further information on the X-ray laboratory is given in [42].

Each cement suspension was tested with 3 different bubble sizes and every bubble size was injected 4 times in a row with a 60 s rest period without mixing between the injections. During this 60 s rest the suspension is allowed to recover and rebuild its structure. The first bubble is referred to as the primary bubble, while the following three bubbles are referred to as the secondary bubbles. The bubbles are enumerated in the sequence of their injection.

2.5. Image-based evaluation of X-ray data

An image-based evaluation process of the data recorded by the X-ray device was developed to assess the bubble properties. After a first image adjustment of the raw images, a threshold-based MATLAB segmentation for air bubble detection was performed. To smooth the image and reduce noise we used a median filter. Finally, a highlighted overlay bounding box over the bubble is created, that determines a rectangle representing the exact height and width of the bubble geometry. Fig. 2 shows the full image evaluation procedure from a recorded raw image (see Fig. 2, left) to an automatically segmented bubble with a coloured bounding box (see Fig. 2, right). The bubble is assumed to be rotationally symmetric, allowing to calculate the bubble volume from its cross section area. The aspect ratio (bubble height divided by bubble width) was used to determine the bubble shape. Furthermore, the centroid of the air bubble and the centroid of the bounding box in both y- and x-direction are measured and can be used for describing the trajectory of each bubble. All parameters are recorded frame-wise, documenting changes in the parameters as a function of ascent time.

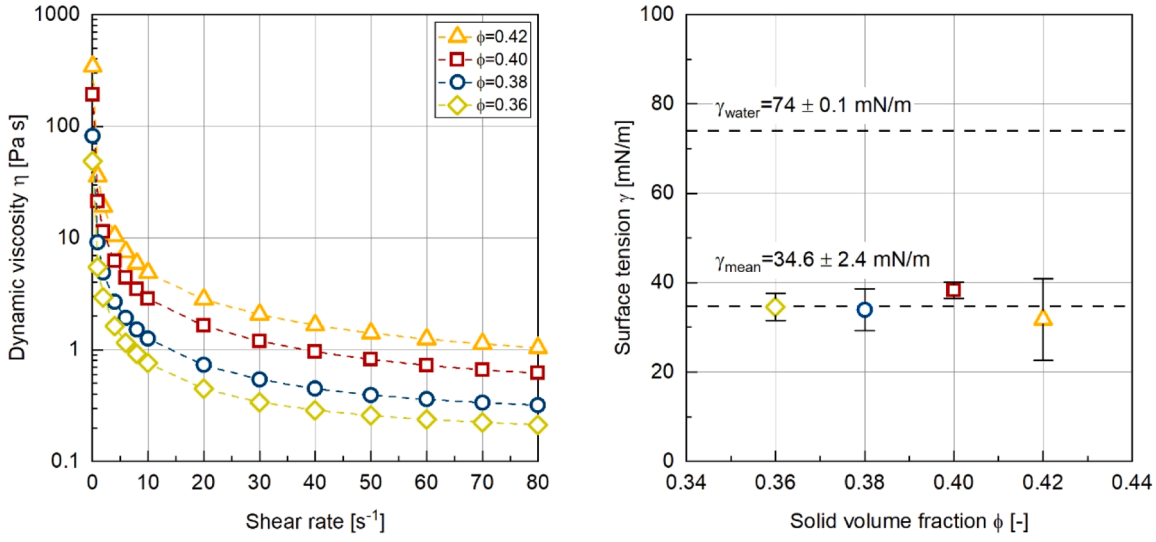

Fig. 3. Dynamic viscosity η as a function of shear rate $\dot{\gamma}$ (left) and surface tension γ as a function of ϕ (right).

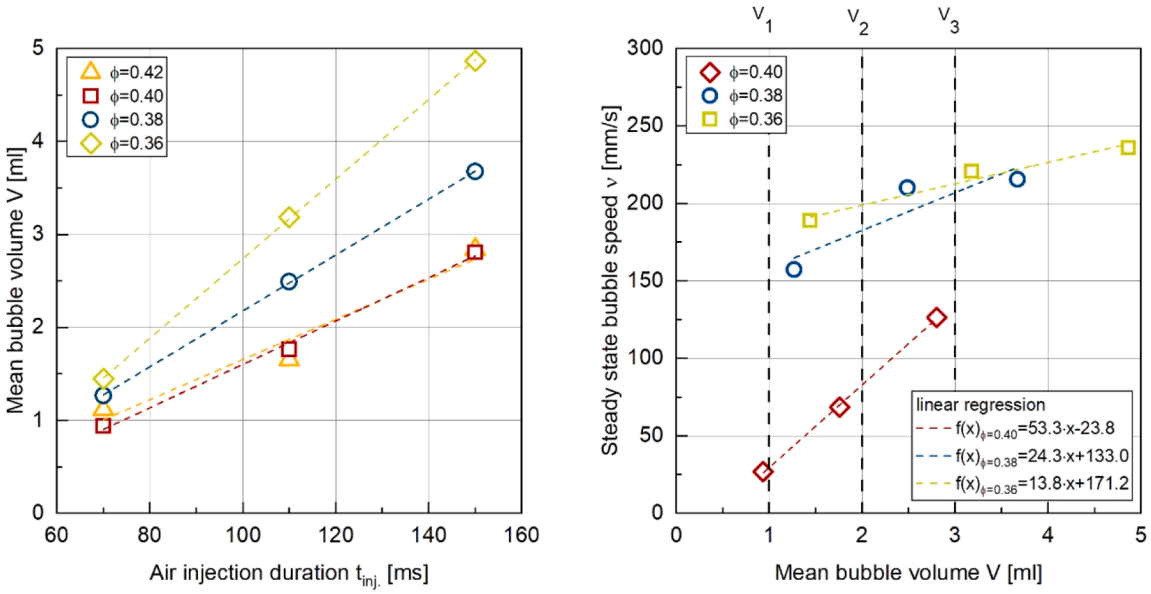

Fig. 4. Mean bubble volume V as a function of air injection duration $t_{inj.}$ for different ϕ (left); steady state bubble speed *v* as a function of the mean bubble volume V (right).

3. Experimental results and discussion

3.1. Suspension characterization

By varying the phase content ϕ of the suspensions, different rheological properties were achieved. Before the X-ray testing, the suspensions were subjected to rheological characterization and surface tension measurements. The results of these experiments are shown in Table 4. Increasing ϕ in the suspension leads to an increase in the yield stress $\tau_{0,rheo}$ from 6.18 Pa to 46.26 Pa and from 0.14 Pa s to 0.47 Pa s for the plastic viscosity μ_{rheo}. As expected, the increase in rheological properties results in a decrease in spread flow diameter from 325.0 mm to 197.5 mm. The Bingham yield stress $\tau_{0,slump}$ calculated from the slump flow using Eq. 2 is in a good linear relation to the yield stress $\tau_{0,rheo}$ measured by the rheometer method. As intended, the suspensions listed in Table 4 cover a broad field of rheological properties for the study of air bubble rise. The suspension density was calculated from the raw materials (Chapter 2.1).

As the Bingham parameter yield stress and plastic viscosity of cement suspensions do not capture the full shear thinning behaviour of the material, Fig. 3, left shows the effect of shear rate on the dynamic viscosity at steady state. The viscosity decreases with both increasing shear rate and decreasing phase content. This data can in a next step be used to directly determine the dynamic viscosity of the suspension during shear caused by a moving air bubble. Looking to the effect of the solid volume fraction onto the surface tension *γ*, no clear trend can be observed. All mean values are in the range of 31.7 mN/m to 38.3 mN/m, showing that the surface tension in good approximation seems to be independent of ϕ, with a mean value of 34.6 mN/m. The standard deviation indicates that the results vary within the scatter range (see Fig. 3, right). For validation purposes, the surface tension of water was measured to be 74 ± 0.1 mN/m with the same device. This value closely corresponds to results reported in the literature with 72.6 ± 0.4 mN/m [43].

3.2. General observations in the de-airing measurements

Before the presentation of the main results of the de-airing tests, several general observations have been made which are important for the interpretation of the results. The air bubble injection mechanism in this setup is time controlled. The injection duration was set to 70, 110 and 150 ms, respectively, for every suspension resulting in different bubble sizes. Fig. 4 shows the volume of the primary bubbles as a function of the injection duration for the suspensions studied. Hereby, it can be seen that different ϕ lead to varying bubble volumes despite the same injection duration. As the surface tension was shown to be nearly constant, this allows for the conclusion, that at constant pressure the bubble formation is primarily controlled by the displacement of the suspension by air, which slows down with increasing dynamic viscosity. As a result, an almost linear correlation between the injection duration and the resulting air bubble volume can be observed for all ϕ.

This dependency of the bubble volume on the paste rheology poses a challenge for the de-airing investigations. In order to be able to study the speed of bubbles of identical volume in different suspensions (i.e. different viscosities), three reference volumes V_1 = 1 ml to V_3 = 3 ml were introduced in Fig. 4, right. Assuming that the bubble speed is proportional to the bubble volume, the measured volume $v_{meas.}$ can be transferred to the above-mentioned corresponding reference volumes V by using the equation of the linear regression in Fig. 4, right.

The image-based evaluation described in Section 2.5 can now be used to quantify the bubble parameters and correlate them with the suspension parameters from Table 4 and Fig. 3. In this study, the bubble speed at steady state *v*, the bubble aspect ratio χ (i.e. height divided by width) and the mean absolute deviation from the primary path β_{MAD} as a parameter for describing the changes in trajectory are considered as main bubble parameters. To ensure that these parameters are not affected by the air injection process, a region of interest starting from 100 mm to 250 mm from the bottom of the sample column was selected and the mean values were computed in this region.

3.3. Trajectory of air bubbles

The trajectory shows the rising path of the air bubble centroid in y- and x-direction during bubble movement. Every graph in Fig. 5 shows the primary bubble as a solid line followed by 3 secondary bubbles in dashed and dotted lines for the constant air injection time of 70 ms. From the qualitative point of view, it can be noted, that the trajectory of all 4 bubbles in the most viscous suspension (ϕ=0.40) is quasi identical. However, for the suspensions with higher flowability (ϕ=0.38 and ϕ=0.36), each bubble takes its own trajectory, without being affected by the previous one. A similar phenomenon has been described by Lopez

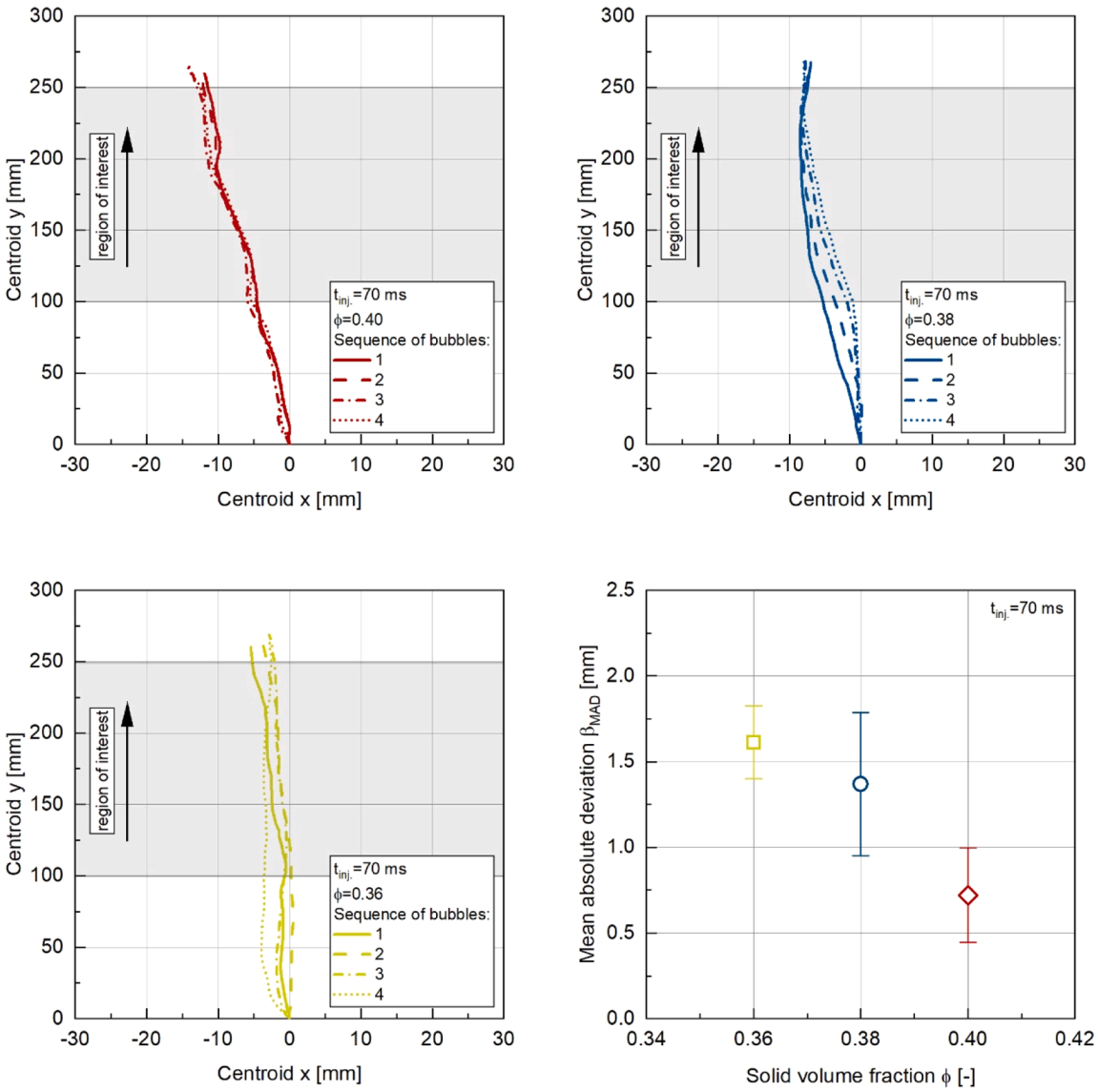

Fig. 5. Trajectory of the primary bubble and three following secondary bubbles for ϕ=0.40 (top left), ϕ=0.38 (top right), ϕ=0.36 (bottom left) and the mean absolute deviation β_{MAD} of the secondary bubbles as a function of ϕ (bottom right).

et al. [25], however for an artificial shearing and a predetermined path. In order to describe this phenomenon quantitatively, we computed the mean absolute deviation from the primary path β_{MAD} of the rising path absolute shortest horizontal distance of every data point of each secondary bubble to its corresponding primary bubble. The β_{MAD} as a function of ϕ shows clearly, that with increasing ϕ the β_{MAD} decreases, indicating that secondary bubbles tend to follow primary bubbles with increasing likeliness for increasing solid volume fraction. The changes in bubble speed and shape due to the same trajectories are shown in the following chapter.

3.4. Bubble rise speed

The bubble rise speed is one of the most important de-airing parameters. The speed is directly related to the bubble volume (see Fig. 4, right) and more importantly to the suspension properties, as can be seen in Fig. 6.

As the dynamic viscosity of cement suspensions is strongly dependent both on the applied shear rate as well as on the shear history, the actual viscosity $\eta(\dot{\gamma})$ experienced by the rising bubble needs to be considered in all calculations. Whereas the influence of the shear rate onto the dynamic viscosity $\eta(\dot{\gamma})$ is well known, realistically determining the shear rate poses a significant challenge, as no clear shear plane can be identified. This challenge has been addressed in the literature e.g. by [27–29] and it is proposed to calculate the characteristic shear rate $\dot{\gamma}_b$ caused in the fluid by the rising air bubble by normalising the bubble rising velocity v by the effective radius r_{eff} of a spherical bubble of the same size. As a result the shear rate $\dot{\gamma}_b$ caused by the bubble rise calculates as shown in Eq. 4.

$$\dot{\gamma}_b = \frac{v}{r_{eff}} \tag{4}$$

Fig. 6, left shows the influence of the dynamic viscosity $\eta(\dot{\gamma}_b)$ on the bubble rise speed in steady state for varying ϕ. As introduced in the general observations (see Section 3.2, Fig. 4, right), the measured bubble speed v was corrected using a linear regression to exclude the effect of the different bubble volumes and ensure the suspension properties as a dominant influencing parameter. This correction is included in the bubble velocity by introducing the factor κ in Fig. 6.

The graph in Fig. 6, left, hereby shows, that increasing the dynamic viscosity results in a significant decrease in bubble speed, until bubble stagnation for ϕ=0.42 for all bubble volumes. It becomes also visible,

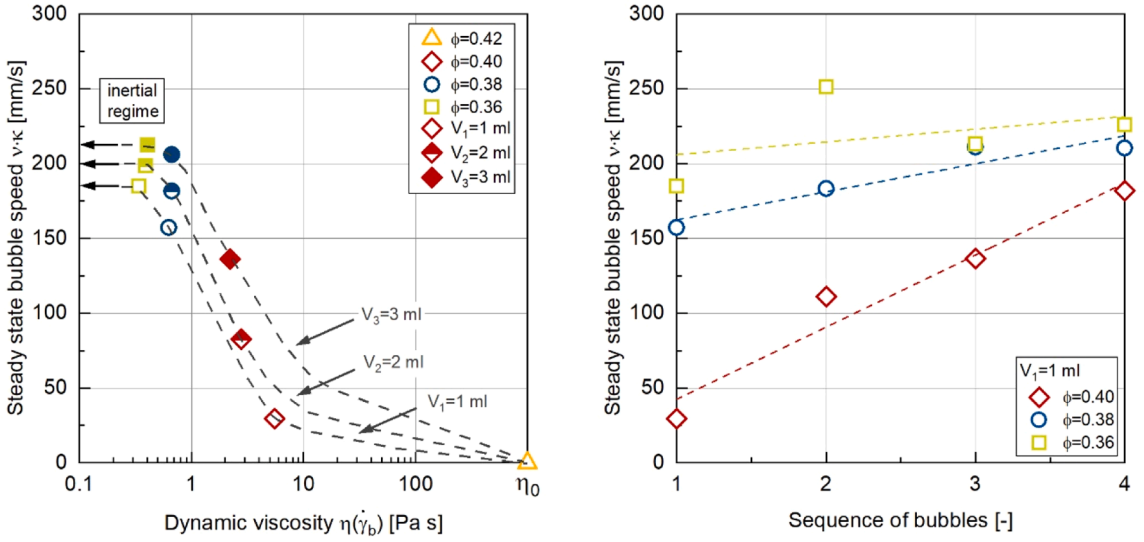

Fig. 6. Steady state bubble speed v as a function of the dynamic viscosity $\eta(\dot{\gamma}_b)$ (left) and v as a function of the sequence of secondary bubbles for a bubble volume of 1 ml (right); The actual v is corrected to the speed of a reference bubble volume by the factor κ.

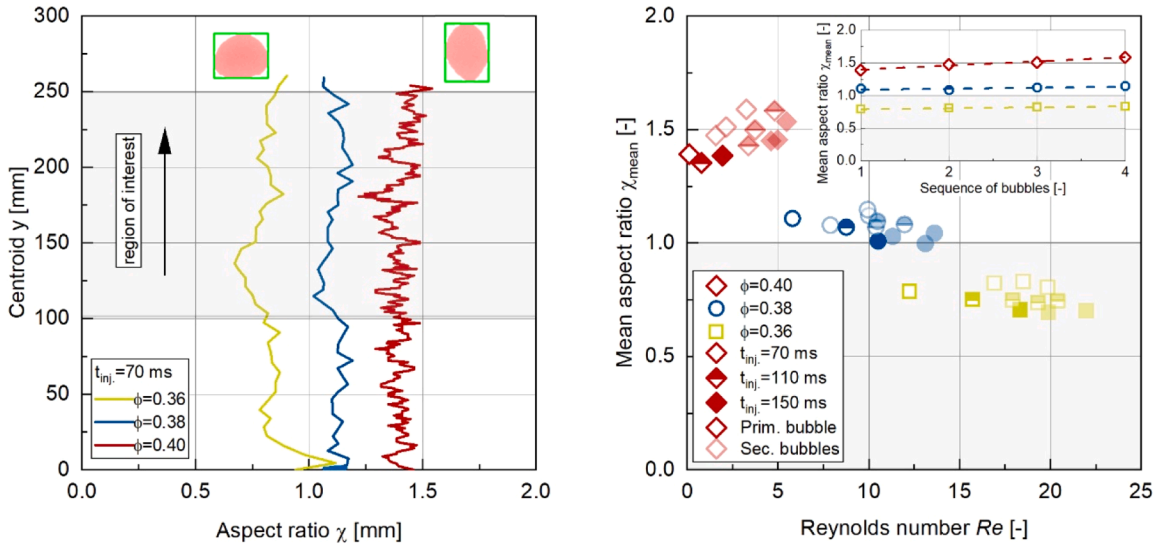

Fig. 7. Changes in aspect ratio χ during the bubble rise in y-direction (left); the gray region indicates the region of interest in which the bubble properties are averaged. χ_{mean} as a function of the Reynolds number Re (right) - and as a function of the sequence of bubbles (right, inset).

that the effect of the viscosity is more dominant between ϕ=0.40 and 0.38, compared to between ϕ=0.38 and 0.36. The data curve points out to be in an S-shape with a plateau for very low viscosities, meaning that in this regime, the viscosity plays a subordinate role. Indeed, at low viscosity, the inertial forces dominate the viscous forces, and the bubble speed becomes independent on the surrounding fluid viscosity. We thus observe, from right to left on Fig. 6, left, the transition between the so-called viscous (right side) and inertial (left side) regimes.

As described in the trajectory results in Section 3.3 before, 3 subsequent bubbles were injected after each primary bubble. Therefore, Fig. 6, right, shows the corresponding bubble speeds, as a function of the sequence of bubbles describing the 4 injected bubbles. It is very clear that for the viscous suspension (ϕ=0.40) the bubble speed increases significantly with each secondary bubble until it reaches almost the same speed as the other suspensions. On the other hand, for the more liquid suspensions (ϕ=0.38 and ϕ=0.36) this phenomenon is less pronounced.

This combined phenomena of the same trajectory and increased bubble speed of the secondary bubbles can be explained as follows: During shear processes in cement suspensions, a slippage layer is formed in the shear zone, which can locally increase the amount of water [44]. In the case of air bubble rise in such suspensions, each bubble generates a shear rate that causes shear-induced particle migration in the rising path that facilitates the rise of subsequent secondary bubbles along this path. Due to locally higher water contents (i.e. lower viscosities) in this path, the bubble speed of the secondary bubbles is increased. The higher the initial particle content of the suspension, the more pronounced this effect.

3.5. Bubble aspect ratio

The aspect ratio χ is used to describe the shape of the bubble. Fig. 7, left, shows the changes in χ during the vertical movement of the bubble centroid. By varying ϕ, χ changes from flattened ($\chi < 1$) to elliptical ($\chi > 1$) bubble shapes, with χ being almost constant during the entire movement. Fig. 7, right, shows the temporal mean value of χ, χ_{mean}, in

the region of interest as a function of the Reynolds number Re (see Eq. 1). The grey area corresponds to $\chi_{mean} \leq 1$ as the transition from the viscous to the inertial flow regime. Qualitatively, the bubble shape seems to follow again an S-shaped function with Re so that χ_{mean} decreases significantly with increasing Re. It is known from the literature that the aspect ratio is directly related to the flow regimes (i.e. inertial and viscous regimes) [45]. The viscous regime is known to start at $\chi_{mean} > 1$ and the inertial regime at $\chi_{mean} < 1$, although there is a continuous transition between the two regimes. In the investigations at hand, the average values of χ_{mean} confirm that the bubble rise in cement suspensions occurs at ϕ=0.40 in the viscous regime, ϕ=0.38 in the transition zone and ϕ=0.36 in the inertial regime. However, it should be noted that the calculated Re are higher than expected from the literature for a detailed separation of the flow regimes.

Moreover, it should be noted that the solid symbols in Fig. 7, right describe the primary bubbles and the transparent symbols the secondary bubbles. In particular, in the more viscous suspension (ϕ=0.40), an increase in χ_{mean} can be observed for a sequence of (secondary) bubbles. This means in effect, that the secondary bubbles become less wide and increased height (i.e. more elliptical). These changes in bubble shape for secondary bubbles were already noted by Mougin et al. [26] and may be related to the formation of a shear channel with regions of reduced particle concentration in the centre and higher particle concentrations with increasing distance from the channels center axis. On the other hand, for the cement suspensions with higher flowability (i.e. ϕ=0.36 and ϕ=0.38) this trend of increasing aspect ratio with each secondary bubble is not present, or rather, the aspect ratio remains constant while the Re number increases. For a better overview, the inset in Fig. 7, right shows the aspect ratio as a function of the sequence of bubbles, which confirms the phenomena mentioned above.

3.6. Modelling of bubble speed

For modelling the bubble speed in homogenous fluids, Stokes' law can be used. It originally describes the drag force of a spherical solid moving through a viscous fluid but it can be adapted to also compute the terminal velocity of a bubble movement in such a medium. Stokes' law can be simplified to the case of low Re numbers when viscous forces are dominant and inertial forces become negligible. Low Re numbers are observed for small object volumes (e.g. by less buoyancy) or in highly viscous fluids (e.g. low rising speed).

The drag force expression for a rising air bubble differs to the one of a solid body by the introduction of a no-slip condition at the interface between the fluid and the bubble. The drag force of a rising bubble F_d can be computed with Eq. 5 as a function of the dynamic viscosity$\eta(\dot{\gamma}_b)$, the radius r and the terminal velocity v of the bubble [17]. The gravitational force F_g acting on the bubble is expressed in Eq. 6 with the density of the fluid ρ_f, the density of the gas inside the bubble ρ_b and the gravitational constant g.

$$F_d = 4 \bullet \pi \bullet \eta(\dot{\gamma}_b) \bullet r \bullet v \tag{5}$$

$$F_g = \frac{4}{3} \bullet \pi \bullet r^3 \bullet (\rho_f - \rho_b) \bullet g \tag{6}$$

During bubble rise, Eqs. 4 and 5 have to be equal resulting in Eq. 7 and then 8.

$$4 \bullet \pi \bullet \eta(\dot{\gamma}_b) \bullet r \bullet v \quad = \quad \frac{4}{3} \bullet \pi \bullet r^3 \bullet \rho_f \bullet g \tag{7}$$

$$v = \frac{1}{3} \bullet \frac{(\rho_f - \rho_b) \bullet g \bullet r^2}{\eta(\dot{\gamma}_b)} \tag{8}$$

In addition to this basic approach, there are two further modifications. Stokes' law is valid for the rise of an air bubble in an infinitely large environment without any recirculations at the walls. In this study, the experimental test column has defined dimensions (i.e. $R = 35$ mm)

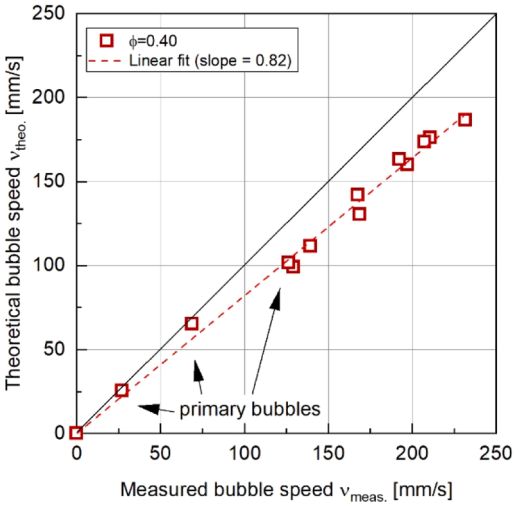

Fig. 8. Theoretical bubble speed according to Eq. 10 against measured bubble speed for ϕ=0.40.

which are considered in relation to the bubble radius r by the following correction in Eq. 9.

$$v = \frac{1}{3} \bullet \frac{(\rho_f - \rho_b) \bullet g \bullet r^2}{\eta(\dot{\gamma}_b)} \bullet \left(1 - 2.1 \bullet \frac{r}{R}\right) \tag{9}$$

As mentioned above, the simplified Stokes' law is valid for low Reynolds numbers (i.e. Re < 1), which is not the case for all bubbles studied. Therefore another modification can be used to include Re in the model approach, which is shown in Eq. 10.

$$v = \frac{1}{3} \bullet \frac{(\rho_f - \rho_b) \bullet g \bullet r^2}{\eta(\dot{\gamma}_b) \bullet \sqrt{1 + \frac{3}{16} \bullet \mathrm{Re}}} \bullet \left(1 - 2.1 \bullet \frac{r}{R}\right) \tag{10}$$

Based on Eq. 10, we computed the theoretical bubble speed $v_{theo.}$ and plotted the latter against the measured bubble speed $v_{meas.}$ in steady state from the experiments (see Fig. 8). The results hereby show a very good correlation, however exhibiting a systematic underestimation of the experimental results (approx. 82 %). Looking more closely at the fundamental formula in Eq. 8, the viscosity is the dominant parameter in the denominator. The viscosity of shear-thinning fluids (e.g. cement suspensions) depends on the shear rate at the bubble interface. The resulting shear rate is in turn calculated by the ratio of bubble speed and a bubble shear length parameter, i.e. the effective radius in this study, which is commonly used but has to be seen as a simplification for modelling. The exact shear rate dependent viscosity distribution around a moving bubble is still part of research and only described to a limited extent [27–29]. Even a small adjustment of the bubble shear length results in non-negligible changes in the shear rate, the viscosity and finally the theoretical bubble speed. This may cause the differences between the theoretical and the experimental measured data in this study.

It is also noteworthy, that for the subsequent bubble data points the values increasingly deviate from the linear regression. On the one hand, as described above, the velocity and hence the Re number of the secondary bubbles increases and exceeds Re > 1. On the other hand, it is assumed that the primary bubble leads to inhomogeneity and particle migration in the shear channel, meaning that the cement suspension can no longer be assumed to be a homogenous effective fluid so that the simplified Stokes' law is not valid as both boundary conditions are no longer completely fulfilled by the secondary bubbles, which is reflected in larger deviations in the predicted velocities.

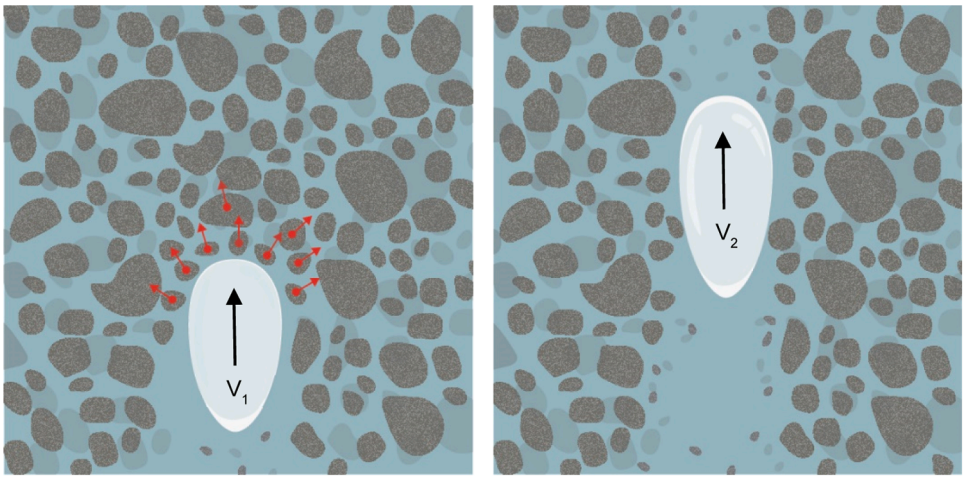

Fig. 9. Theoretical model concept of shear-induced particle migration and channelling effect for the rise of primary bubbles (left) and subsequent bubbles (right) in a cement suspension.

4. Conclusions

In this paper, we have observed how single air bubbles of different volumes rise in cement suspensions with different rheological properties. A new experimental setup consisting of a rise column with a bubble injection device was combined with in-situ X-ray imaging, allowing the measurement of both bubble geometry as well as speed. In particular, the influence of different solid volume fractions ϕ on bubble speed, bubble shape, and trajectory was investigated. A key point of interest has been the effect of the shear history, meaning the rise of subsequent bubbles and how each bubble is affected by the previous one.

The investigations show that the rise behaviour of air bubbles in cement suspensions can be categorized into three different regimes, i.e. a inertial, a transient and a viscous flow regime. The presence of these different flow regimes means that the viscosity of the suspension is not the sole parameter controlling bubble rise, and inertial forces must be taken into account. The bubble speed and the bubble aspect ratio show the same Re number dependence known for other homogeous fluids such as carbopol for the transition in the inertial ($Re >> 1$, $\chi_{mean} \leq 1$) to viscous ($Re \leq 1$, $\chi_{mean} > 1$) regimes.

New experimental results have been obtained for the rise of subsequent bubbles. In the viscous regime, the secondary bubbles follow the same trajectory, rise faster and the aspect ratio increases compared to the primary bubble. The reasons for this may be related to shear-induced particle migration in the rising path, resulting in locally higher amounts of water and lower viscosities which in turn allows for easier rise of the following bubbles. A theoretical model concept of such shear-induced particle migration between the primary (left) and secondary bubble (right) is shown in Fig. 9.

These new findings may raise questions about the use of dimensionless parameters such as the Re number to describe secondary bubble flow, as we need to take into account inhomogeneities and changes in the viscosity due to shear-induced particle migration described above. The physics behind bubble rise in fluids and suspensions is also only valid for homogeneous systems, which is not the case when considering a secondary bubble flow. From this point of view, the effect of particle migration and whether there is a zone with less concentrated regions in the center of the uprising path are still unknown and remain open scientific questions.

Another open question arises from the transition from cement suspensions to fresh concrete with coarse aggregates. However, the rheological behaviour of fresh concrete is mainly controlled by the rheological behaviour of the cement suspension [11], the addition of coarse aggregates has a significant effect on its rheology and probably on the motion of air bubbles through such a coarse grain suspension. In this joint research project we have also investigated the effect of aggregates in different sizes and size distributions for varying ϕ, but these results will be presented in further publications.

CRediT authorship contribution statement

Valérie Vidal: Writing – review & editing, Supervision, Methodology. **Marcus Zuber:** Software, Investigation. **Tobias Schack:** Writing – review & editing, Methodology. **Michael Haist:** Writing – review & editing, Supervision, Methodology, Funding acquisition. **Bastian Strybny:** Writing – original draft, Visualization, Methodology, Investigation, Data curation, Conceptualization. **Julian Link:** Writing – review & editing. **Max Coenen:** Writing – review & editing, Visualization, Software.

Declaration of Competing Interest

The authors declare the following financial interests/personal relationships which may be considered as potential competing interests: Prof. Dr.-Ing. Michael Haist reports financial support was provided by Deutsche Forschungsgemeinschaft (DFG). If there are other authors, they declare that they have no known competing financial interests or personal relationships that could have appeared to influence the work reported in this paper.

Acknowledgements

This research was funded by Deutsche Forschungsgemeinschaft (DFG) under the grants HA 7917/8–1, LU 1652/48–1 SCHA 1854/7–1 and within the DFG priority program 2005 “Opus Fluidum Futurum—Rheology of reactive, multiscale, multiphase construction materials”.

Conflict of interest

The authors have no conflicts of interest to declare that are relevant to the content of this article.

Data Availability

Data will be made available on request.

References

[1] A.R. Cusens, The influence of amplitude and frequency in the compaction of concrete by table vibration, Mag. Concr. Res. (1958) 79–86.
[2] American Concrete Institute - Reported by ACI Committee 309, Report on Behavior of Fresh Concrete During Vibration: ACI 309.1R-08.
[3] G.H. Tattersall, P.H. Baker, The effect of vibration on the rheological properties of fresh concrete, Mag. Concr. Res. 40 (143) (1988).
[4] R.H.H. Kirkham, A.C. Whiffin, The compaction of concrete slabs by surface vibration: first series of experiments, Mag. Concr. Res. 1 (3) (1949) 141–143.
[5] R.D. Davies, Some experiments on the compaction of concrete by vibration, Mag. Concr. Res. (1951) 71–78.
[6] Z. Li, G. Cao, Rheological behaviors and model of fresh concrete in vibrated state, Cem. Concr. Res. 120 (2019) 217–226, https://doi.org/10.1016/j.cemconres.2019.03.020.
[7] P.F.G. Banfill, M.A.O.M. Teixeira, R.J.M. Craik, Rheology and vibration of fresh conrete: Predicting the radius of poker vibrators from wave propagation, Cem. Concr. Res. (41) (2011) 932–941.
[8] G. Grampeix, N. Roussel, and J. Dupoirier, "Intertal vibration and viscous concrete: Application and prediction of the radius of action," 123 - 130.
[9] I. Navarrete, M. Lopez, Estimating the segregation of concrete based on mixture design and vibratory energy, Constr. Build. Mater. 122 (2016) 384–390, https://doi.org/10.1016/j.conbuildmat.2016.06.066.
[10] J.A. Koch, D.I. Castaneda, R.H. Ewoldt, D.A. Lange, Vibration of fresh concrete understood through the paradigm of granular physics, Cem. Concr. Res. 115 (2019) 31–42, https://doi.org/10.1016/j.cemconres.2018.09.005.
[11] C.F. Ferraris, J.M. Gaidis, Connection between the rheology of concrete and rheology of cement paste, MJ 89 (4) (1992), https://doi.org/10.14359/2575.
[12] J. Hu, K. Wang, Effect of coarse aggregate characteristics on concrete rheology, Constr. Build. Mater. 25 (3) (2011) 1196–1204, https://doi.org/10.1016/j.conbuildmat.2010.09.035.
[13] P.F.G. Banfill, Ed., The rheology of fresh cement and concrete - a review, 2003.
[14] F. de Larrard, C.F. Ferraris, T. Sedran, Fresh concrete: A Herschel-Bulkley material, Mater. Struct. 31 (1998) 494–498.
[15] G.H. Tattersall, P.F. Banfill, The Rheology Of Fresh Concrete, Pitman, Boston, 1983.
[16] N. Roussel, G. Ovarlez, S. Garrault, C. Brumaud, The origins of thixotropy of fresh cement pastes, Cem. Concr. Res. 42 (1) (2012) 148–157, https://doi.org/10.1016/j.cemconres.2011.09.004.
[17] R. Clift, J.R. Grace, M.E. Weber, Bubbles, Drops, and Particles, Dover Publ, Mineola, NY, 2013.
[18] J.F. Harper, The motion of bubbles and drops through liquids. Advances in Applied Mechanics, Advances in Applied Mechanics Volume 12, Elsevier, 1972, pp. 59–129.
[19] T. Maxworthy, C. Gnann, M. Kürten, F. Durst, Experiments on the rise of air bubbles in clean viscous liquids, J. Fluid Mech. 321 (1996) 421–441, https://doi.org/10.1017/S0022112096007781.
[20] G. Astarita, G. Apuzzo, Motion of gas bubbles in non-Newtonian liquids, AIChE J. 11 (5) (1965) 815–820, https://doi.org/10.1002/aic.690110514.
[21] N. Dubash, I. Frigaard, Conditions for static bubbles in viscoplastic fluids, Phys. Fluids 16 (12) (2004) 4319–4330, https://doi.org/10.1063/1.1803391.
[22] N. Dubash, I.A. Frigaard, Propagation and stopping of air bubbles in Carbopol solutions, J. Non-Newton. Fluid Mech. 142 (1-3) (2007) 123–134, https://doi.org/10.1016/j.jnnfm.2006.06.006.
[23] M.K. Tripathi, K.C. Sahu, G. Karapetsas, O.K. Matar, Bubble rise dynamics in a viscoplastic material, J. Non-Newton. Fluid Mech. 222 (2015) 217–226, https://doi.org/10.1016/j.jnnfm.2014.12.003.
[24] J. TSAMOPOULOS, Y. DIMAKOPOULOS, N. CHATZIDAI, G. Karapetsas, M. Pavlidis, Steady bubble rise and deformation in Newtonian and viscoplastic fluids and conditions for bubble entrapment: TSAMOPOULOS, J.; DIMAKOPOULOS, Y.; CHATZIDAI, N.; Karapetsas, G.; PAVLIDIS, M, J. Fluid Mech. 601 (2008) 123–164, https://doi.org/10.1017/S0022112008000517.
[25] W.F. Lopez, M.F. Naccache, P.R. de Souza Mendes, Rising bubbles in yield stress materials, J. Rheol. 62 (1) (2018) 209–219, https://doi.org/10.1122/1.4995348.
[26] N. Mougin, A. Magnin, J.-M. Piau, The significant influence of internal stresses on the dynamics of bubbles in a yield stress fluid, J. Non-Newton. Fluid Mech. 171-172 (2012) 42–55, https://doi.org/10.1016/j.jnnfm.2012.01.003.
[27] A. Fakhari, C. Fernandes, Single-bubble rising in shear-thinning and elastoviscoplastic fluids using a geometric volume of fluid algorithm, Polymers 15 (16) (2023), https://doi.org/10.3390/polym15163437.
[28] S. Li, Y. Ma, T. Fu, C. Zhu, H. Li, The viscosity distribution around a rising bubble in shear-thinning non-newtonian fluids, Braz. J. Chem. Eng. 29 (2) (2012) 265–274, https://doi.org/10.1590/S0104-66322012000200007.
[29] L. Zhang, C. Yang, Z.-S. Mao, Numerical simulation of a bubble rising in shear-thinning fluids, J. Non-Newton. Fluid Mech. 165 (11-12) (2010) 555–567, https://doi.org/10.1016/j.jnnfm.2010.02.012.
[30] N. Hooshyar, J.R. van Ommen, P.J. Hamersma, S. Sundaresan, R.F. Mudde, Dynamics of single rising bubbles in neutrally buoyant liquid-solid suspensions, Phys. Rev. Lett. 110 (24) (2013) 244501, https://doi.org/10.1103/PhysRevLett.110.244501.
[31] C. Madec, B. Collin, J. John Soundar Jerome, S. Joubaud, Puzzling bubble rise speed increase in dense granular suspensions, Phys. Rev. Lett. 125 (7) (2020) 78004, https://doi.org/10.1103/PhysRevLett.125.078004.
[32] G.K. Auernhammer, et al., Transparent model concrete with tunable rheology for investigating flow and particle-migration during transport in pipes, Mater. Des. 193 (2020) 108673, https://doi.org/10.1016/j.matdes.2020.108673.
[33] DIN EN 1097-7:2008-06, Tests for mechanical and physical properties of aggregates - Part 7: Determination of the particle density of filler - Pyknometer method; German version EN 1097-7:2008, Berlin.
[34] DIN ISO 9277:2014-01, Determination of the specific surface area of solids by gas adsorption - BET method (ISO 9277:2010), Berlin.
[35] DIN EN 196-6:2019-03, Methods of testing cement - Part 6: Determination of fineness; German version EN 196-6:2018, Berlin.
[36] U. Pott, et al., Characterization data of reference materials used for phase II of the priority program DFG SPP 2005 "Opus Fluidum Futurum - Rheology of reactive, multiscale, multiphase construction materials, Data Brief. 47 (2023) 108902, https://doi.org/10.1016/j.dib.2023.108902.
[37] M. Haist, et al., Interlaboratory study on rheological properties of cement pastes and reference substances: comparability of measurements performed with different rheometers and measurement geometries, Mater. Struct. 53 (4) (2020), https://doi.org/10.1617/s11527-020-01477-w.
[38] N. Roussel, P. Coussot, Fifty-cent rheometer" for yield stress measurements: From slump to spreading flow, J. Rheol. 49 (3) (2005) 705–718, https://doi.org/10.1122/1.1879041.
[39] N. Roussel (Ed.), Understanding the rheology of concrete, Woodhead Publ, Oxford, 2012.
[40] N. Roussel, C. Stefani, R. Leroy, From mini-cone test to Abrams cone test: measurement of cement-based materials yield stress using slump tests, Cem. Concr. Res. 35 (5) (2005) 817–822, https://doi.org/10.1016/j.cemconres.2004.07.032.
[41] M. Haist, Zur Rheologie und den Wechselwirkungen bei Zementsuspensionen. Dissertation, Institut für Massivbau und Baustofftechnologie (IMB), Universität Karlsruhe, (TH), Karlsruhe, 2009.
[42] M. Zuber, Development, Characterization and Application of a novel X-ray Imaging Laboratory," Dissertation, Institute for Photon Science and Synchrotron Radiation, Karlsruhe Institute of Technology, Karlsruhe, 2023.
[43] N.B. Vargaftik, B.N. Volkov, L.D. Voljak, International tables of the surface tension of water, J. Phys. Chem. Ref. Data 12 (3) (1983) 817–820, https://doi.org/10.1063/1.555688.
[44] J. Link, et al., Mechanisms of thixotropy in cement suspensions considering influences from shear history and hydration, ce Pap. 6 (6) (2023) 698–704, https://doi.org/10.1002/cepa.2810.
[45] T. Maxworthy, Bubble formation, motion and interaction in a Hele-Shaw cell, J. Fluid Mech. 173 (1986) 95–114, https://doi.org/10.1017/S002211208600109X.